

Supplementary Information for**Cell atlas of the human ocular anterior segment: Tissue-specific and shared cell types**

Tavé van Zyl, Wenjun Yan, Alexi M. McAdams, Aboozar Monavarfeshani, Gregory S. Hageman, and Joshua R. Sanes

T. van Zyl

Email: tave.vanzyl@yale.edu

J.R. Sanes

Email: sanesj@mcb.harvard.edu

This PDF file includes:

Supplementary methods

Figures S1 to S8

Tables S1 to S3

Legend for Dataset S1

SI References

Other supplementary materials for this manuscript include the following:

Dataset S1

Supplementary Methods

Tissue Acquisition, Dissection and Processing. Human ocular tissues used for sequencing, immunohistochemistry (IHC) and *in situ* hybridization were obtained from Massachusetts General Hospital in collaboration with the Rapid Autopsy Program, Susan Eid Tumor Heterogeneity Initiative and The Lion's Eye Bank in Murray, Utah. Eyes were collected a median of 6 hours postmortem (range 3.5-14hrs; see **Table S1**). Whole globes were transported to either Harvard University or the University of Utah in a humid chamber on ice and processed within an hour of enucleation.

Other human corneoscleral buttons used for IHC were provided by the Lions Vision Gift (Portland, OR) and were collected <16 hr postmortem and fixed in ice-cold 4% PFA. No ocular disease was reported in any of the human donors and no abnormalities were noted during microdissection. Donor details are provided in **Table S2**.

Because race/ethnicity contributes significantly to disease risk in many cases, we hoped to collect tissues from a diversity of racial/ethnic backgrounds. However, owing to the difficulty of obtaining and freezing non-diseased post-mortem ocular tissue with minimum delay, we were only able to obtain tissue from Caucasian donors.

Dissection was performed under a surgical microscope. To isolate the anterior segment, a surgical blade was used to make a small stab incision ~4 mm posterior to the limbus at the pars plana. The incision was extended circumferentially with curved scissors to yield a separated anterior segment and posterior segment. Each segment was placed in a petri dish filled with AMES' medium equilibrated with 95% O₂/5% CO₂, or sterile PBS, on ice.

The anterior segment was further dissected into its component tissues. The lens was liberated from the ciliary body by cutting the zonular attachments with curved microscissors. The lens capsule and superficial lens cells were isolated by making a small curvilinear incision in the anterior lens capsule with a surgical blade, and prolapsing the lens nucleus and cortical material, which was then discarded. The ciliary body was separated from the iris via blunt dissection with forceps and was then divided into 4 equal parts. The iris was divided similarly. After trephination of the central cornea using a 6 mm corneal punch, the remaining corneoscleral rim was addressed. Any large portions of ciliary muscle left behind after blunt dissection of the iris and ciliary body were trimmed off with microscissors. The trabecular meshwork was gently freed from the corneoscleral rim, often in multiple strips, by inserting one prong of the microforceps into Schlemm's canal and gently clamping onto the trabecular meshwork tissue with the other prong and applying steady traction. The remaining corneoscleral tissue was cut into wedges and each wedge was trimmed to include approximately 1-2 mm of peripheral cornea and 1-2 mm of perilimbal sclera.

For disease gene interrogation, five human macular samples were also dissected using an 8mm punch centered on the fovea (see **Table S1**).

For snRNA-seq, each dissected tissue was immediately placed along the wall of a cryogenic vial, ensuring minimal liquid was present, and submerged in dry ice or liquid nitrogen. For long-term storage, the cryogenic vials were moved to a -80°C freezer. Samples collected at the University of Utah were transferred to Harvard University via overnight shipping on dry ice. For single-nuclei isolation, frozen tissue samples were homogenized in a dounce homogenizer with NP-40 (0.1%) Tris-based lysis buffer and passed through a 40-μm cell strainer. The filtered nuclei were then pelleted at 500 rcf over 5 min and resuspended in 2% BSA with DAPI counterstain for cell sorting on a flow cytometer to remove cellular debris. The sorted nuclei were pelleted again at 500 rcf over 5 min and resuspended in 0.04% non-acetylated BSA/PBS solution and adjusted to a concentration of 1000 nuclei/μL. The integrity of the nuclear membrane and presence of non-nuclear material were assessed under a brightfield microscope before loading into a 10X Chromium Single Cell Chip with a targeted recovery of 6000 nuclei.

Single nuclei libraries were generated with either Chromium 3' V3, or V3.1 platform (10X Genomics, Pleasanton, CA) following the manufacturer's protocol. Briefly, single nuclei were partitioned into Gel-beads-in-EMulsion (GEMs) where nuclear lysis and barcoded reverse transcription of RNA would take place to yield full-length cDNA; this was followed by amplification, enzymatic fragmentation and 5' adaptor and sample index attachment to yield the final libraries.

RNA Sequencing and Data Analysis. Libraries were sequenced on Illumina HiSeq 2500 at the Broad Institute or NovaSeq at the Bauer Core Facility at Harvard University. The single nuclei RNA sequencing data were demultiplexed and aligned using Cell Ranger software (version 4.0.0, 10X Genomics, Pleasanton, CA). Reads were aligned to the human genome GRCh38 version 101 with the following modifications: 1. Human genome files GRCh38 were downloaded from Ensembl; 2. the "transcript" lines in the .gtf file were converted into "exon" lines without changes to the remaining; 3. The reference files were generated using the cellranger "mkref" function; 4. Reads were aligned to the modified file and counted using cellranger "count" function with the chemistry option specified as "SC3PV3".

The downstream analysis pipeline was similar to that in van Zyl et al. with the exception that the R package "Seurat" (version 4.0.3) was used (1). Data from each tissue region was first analyzed separately. Briefly, the count matrix was filtered so only cells with more than 1000 genes detected were included. The dataset was then split into batches based on the donors of the samples and normalized individually using SCTransform. The top 2000 features common across batches were used to identify anchors for data integration. It was then scaled, and principal component (PC) analysis was performed. The top 50 PCs were selected for visualization and clustering. An array of different resolutions was assessed when clustering. Starting with the high resolutions, clusters were evaluated based on number of differentially expressed (DE) genes between closely related clusters. The clustering with maximal resolutions and strong DE genes (more than five DE genes on both up- or down- regulated side between closely related clusters) were, in most cases, taken as the putative types. However, in some cases as pointed out in the text, sub-clustering among certain population was identified only with the higher resolution, and that was projected into the final clustering result. DE test was performed using the "MAST" method. Transcriptomic relationship among clusters was built using the scaled data after integration.

For the anterior segment integrated analysis, a downsampling procedure was introduced so a maximum of 1000 cells from each putative type in each tissue were merged into a combined dataset and re-analyzed. Only contiguous tissues that were spatially and transcriptomically close to each other were included; this excluded the lens. For technical reasons, we also omitted ~1000 cells from the CSW dataset. In assessing the expression of disease related genes in the eye, both the lens and from retinal datasets were subsequently included for completeness. The disease gene lists were generated from the following sources: Disc Diameter and VCDR from (2); POAG from (3); IOP from (4); Myopia from (5); Astigmatism from the National Human Genome Research Institute-European Bioinformatics Institute (NHGRI-EBI) GWAS catalog (downloaded 20 February 2021) (6); and Cataract from the Cat-Map database filtered for genes with documented human phenotypes (<https://cat-map.wustl.edu/>) (7). Only genes that were expressed in more than 25% of cells in any cluster were included in the analysis. To visualize the expression of each disease gene set, a gene set score was calculated as follows: 1. The genes in the gene set list were first filtered so only those that expressed in more than 25% of cells in any putative type were assessed. 2. For each cell i , the mean expression value of the genes in the set j ($\overline{Exp}_{i,j}$) and that of the total transcripts (\overline{Exp}_i) were calculated. 3. The score of gene set j in cell i ($\overline{S}_{i,j}$) was calculated as $\overline{S}_{i,j} = \overline{Exp}_{i,j} - \overline{Exp}_i$. 4. The averaged score of gene set j in each putative type was visualized in Figure 6D and *SI Appendix*, Fig. S7B.

Histology. Corneoscleral wedges or whole globes were fixed in 4% paraformaldehyde in PBS for 2-24 hr and then transferred to PBS. The fixed samples were sunk in 30% sucrose in PBS overnight at 4°C, then embedded in tissue freezing medium and mounted onto coated slides in

10-50 μ m meridional sections with ProLong Gold Antifade Mountant. For immunohistochemistry, slides were incubated for 1 hour in 5% donkey serum and 0.3% TritonX block at room temperature, overnight with primary antibodies in Renoir Red Diluent at 4°C, and 2 hours with secondary antibodies in 3% donkey serum and 0.3% TritonX at room temperature. Antibodies used are listed in **Table S3**. Single molecule fluorescent *in situ* hybridization was performed using commercially available RNAscope Multiplex Fluorescent Assay V2 (Advanced Cell Diagnostics, Newark, CA). Briefly, slides were baked in a HybEZ oven (Advanced Cell Diagnostics, Newark, CA) at 60°C for 30 minutes, then tissue freezing medium was removed by soaking the slides in sterile PBS. A 1-hour post-fix in 4% PFA was performed at 4°C and the slides were then dehydrated in serial ethanol concentration rinses. The slides were incubated for 10 minutes at room temperature with the hydrogen peroxide provided in the assay kit diluted 1:1 in water then for 30 minutes with protease III at 40°C. Probe hybridization and subsequent steps were per standard manufacturer protocol. Probes used are listed in **Table S3**.

Image acquisition, processing and analysis. Images were acquired on Zeiss LSM 710 confocal microscopes with 405, 488-515, 568, and 647 nm lasers, processed using Zeiss ZEN software suites, and analyzed using ImageJ (NIH). Images were acquired with 16X, 40X or 63X oil lenses at the resolution of 1024X1024 pixels, a step size of 0.5-1.5 μ m, and 90 μ m pinhole size.

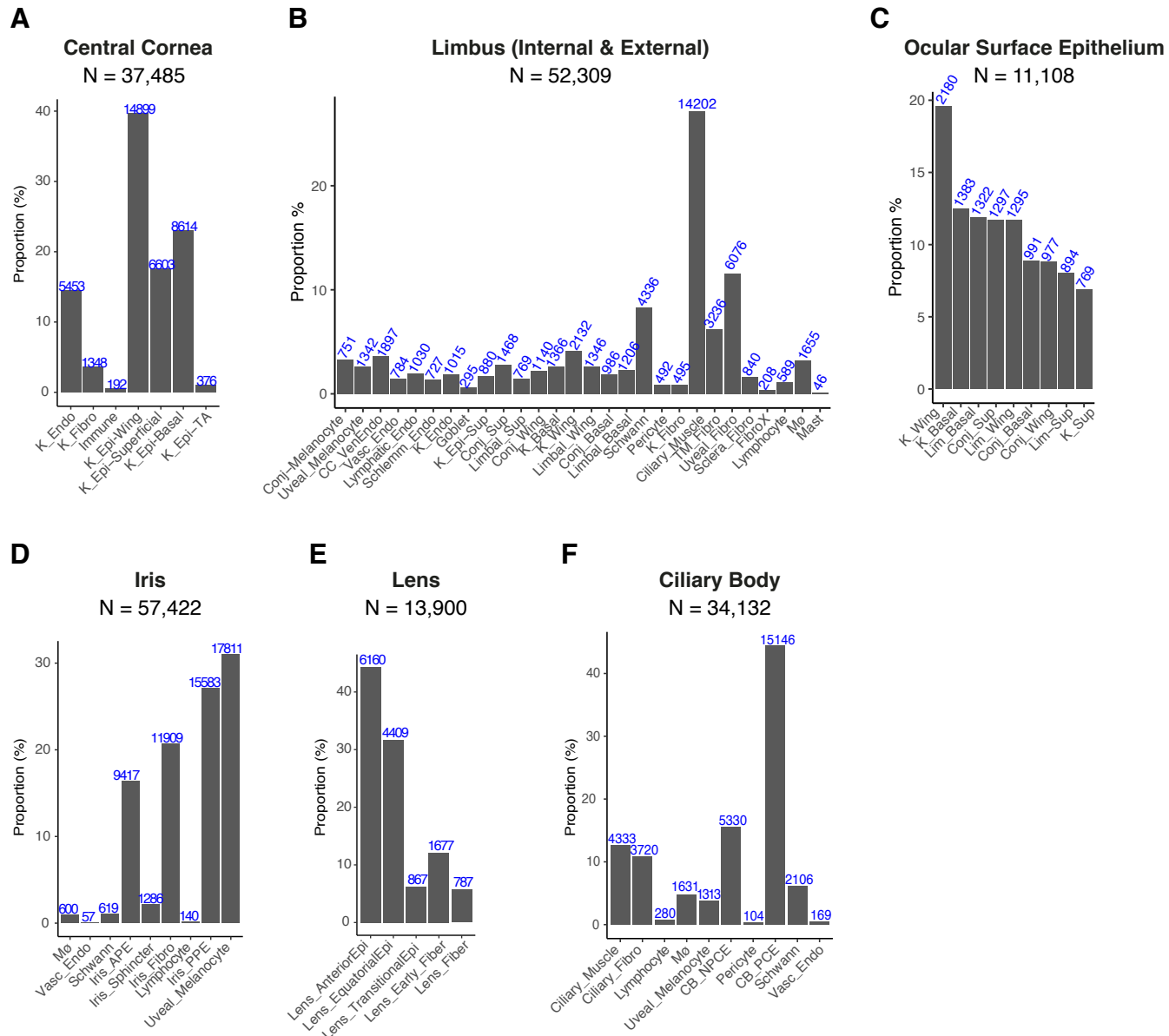


FIG. S1. Distribution of cell types within each tissue. Histograms show percentage of cells assigned to each type in each tissue (A) Central cornea. (B) Internal and external limbus. (C) Limbal ocular surface epithelium (subset of B). (D) Iris. (E) Lens (F) Ciliary body

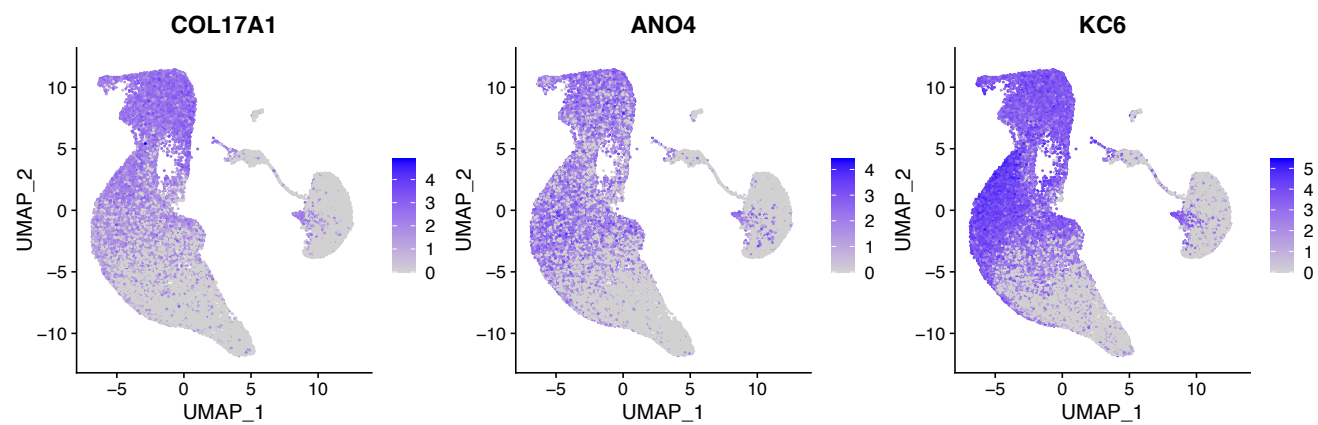
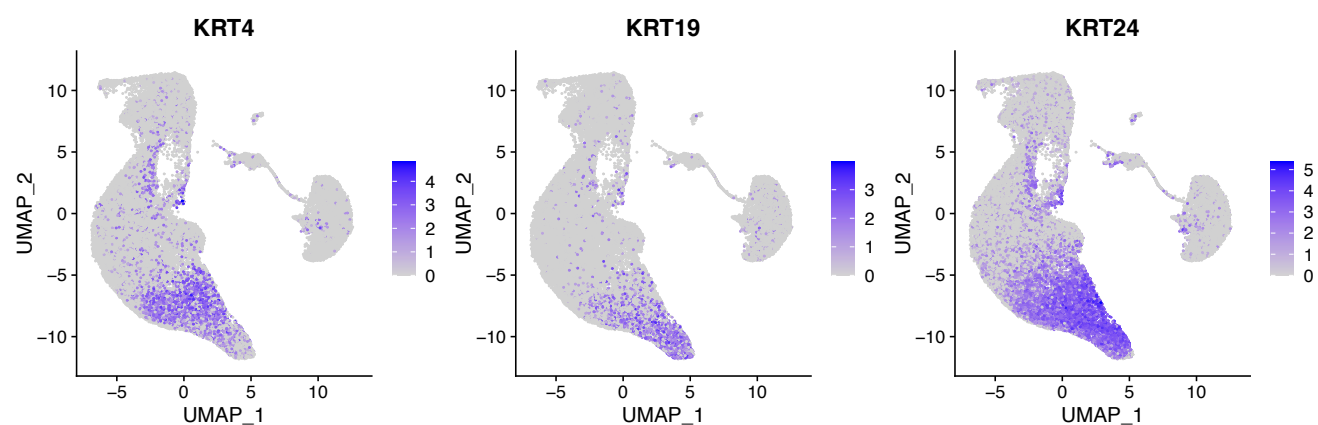
A**B**

FIG. S2. Expression patterns of central corneal epithelium. (A) Feature plots showing gradient expression of COL17A1, ANO4 and KC6 along the basal-superficial axis. Cluster distinctions and annotations are shown in Fig. 1D. (B) Feature plots showing selective expression of KRT4, KRT19 and KRT24 in the superficial epithelium.

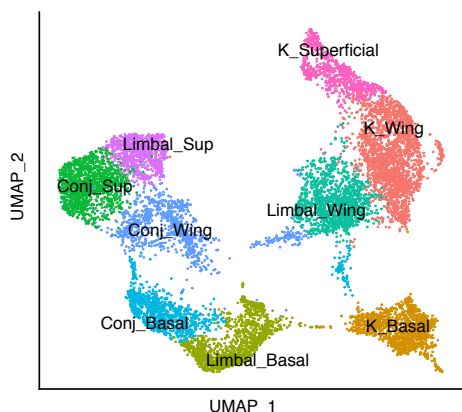
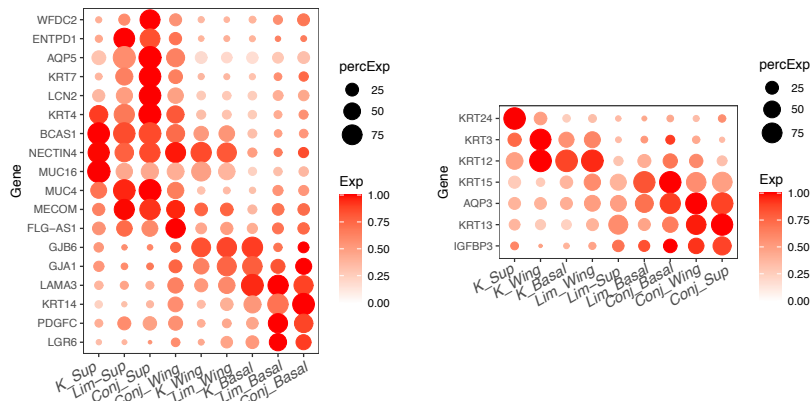
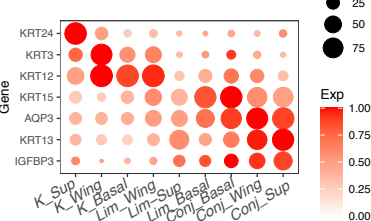
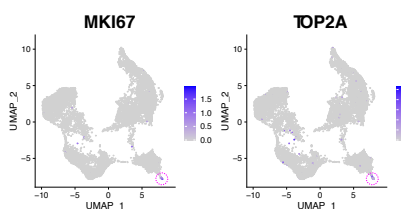
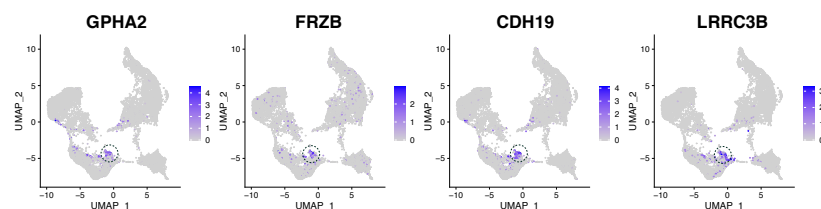
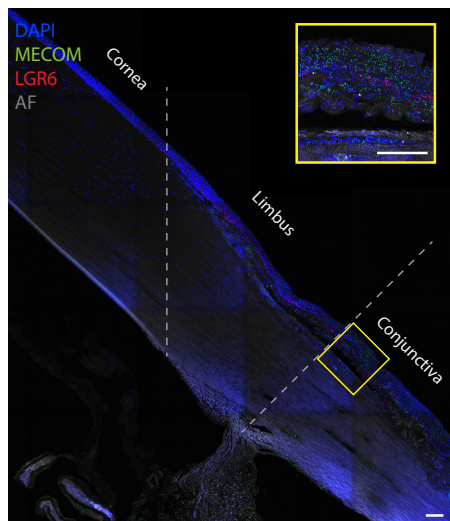
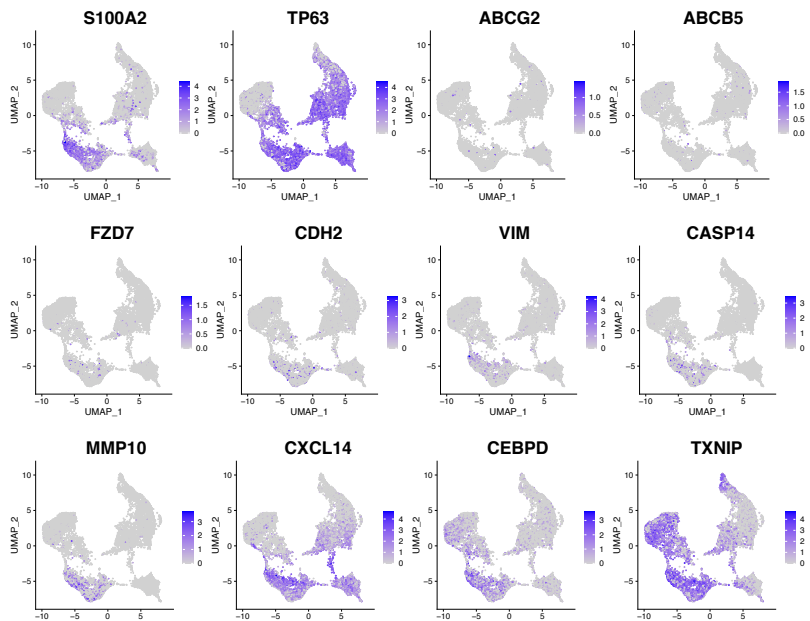
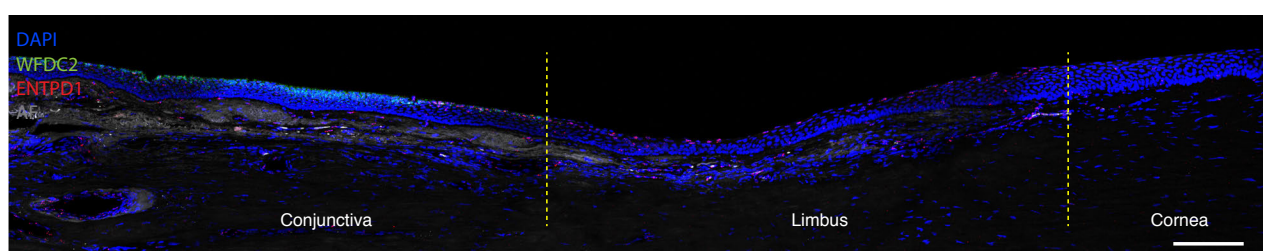
A**B****C****D****E****F****G****H**

Fig. S3. Cell types within the Ocular Surface Epithelium (External Limbus). (A) Clustering of 11,108 single-nucleus transcriptomes derived from corneoscleral wedge tissue that were identified as ocular surface epithelial cells. Data visualized by Uniform Manifold Approximation and Projection (UMAP). (B) Dot plot demonstrating shared expression patterns among superficial, wing and basal cells. (C) Dot plot demonstrating shared expression patterns of cornea, limbal and conjunctival cells. (D) Feature plots showing co-expression of MKI67 and TOP2A, genes associated with mitotically active cells. Pink dashed circle identifies putative transit-amplifying cells as an island within the corneal basal epithelium cluster. (E) Feature plots showing expression of genes associated with limbal progenitor cells (LPC). Green dashed circle identifies putative LPCs as a lobe within the limbal basal epithelium cluster. (F) Composite image of limbal region with dashed lines approximating regions of the cornea, limbus and conjunctiva with underlying sclera. Boxed area is magnified to show LGR6-positive (red) conjunctival basal epithelial cells and MECOM-positive wing and superficial cells visualized with fluorescent RNA in situ hybridization. (G) Feature plots showing expression of genes associated with limbal stem cells and LPCs. (H) RNA in situ hybridization for WFDC2 (green) and ENTPD1 (red) supports distinction of the limbal superficial epithelium from the corneal and conjunctival superficial epithelium.

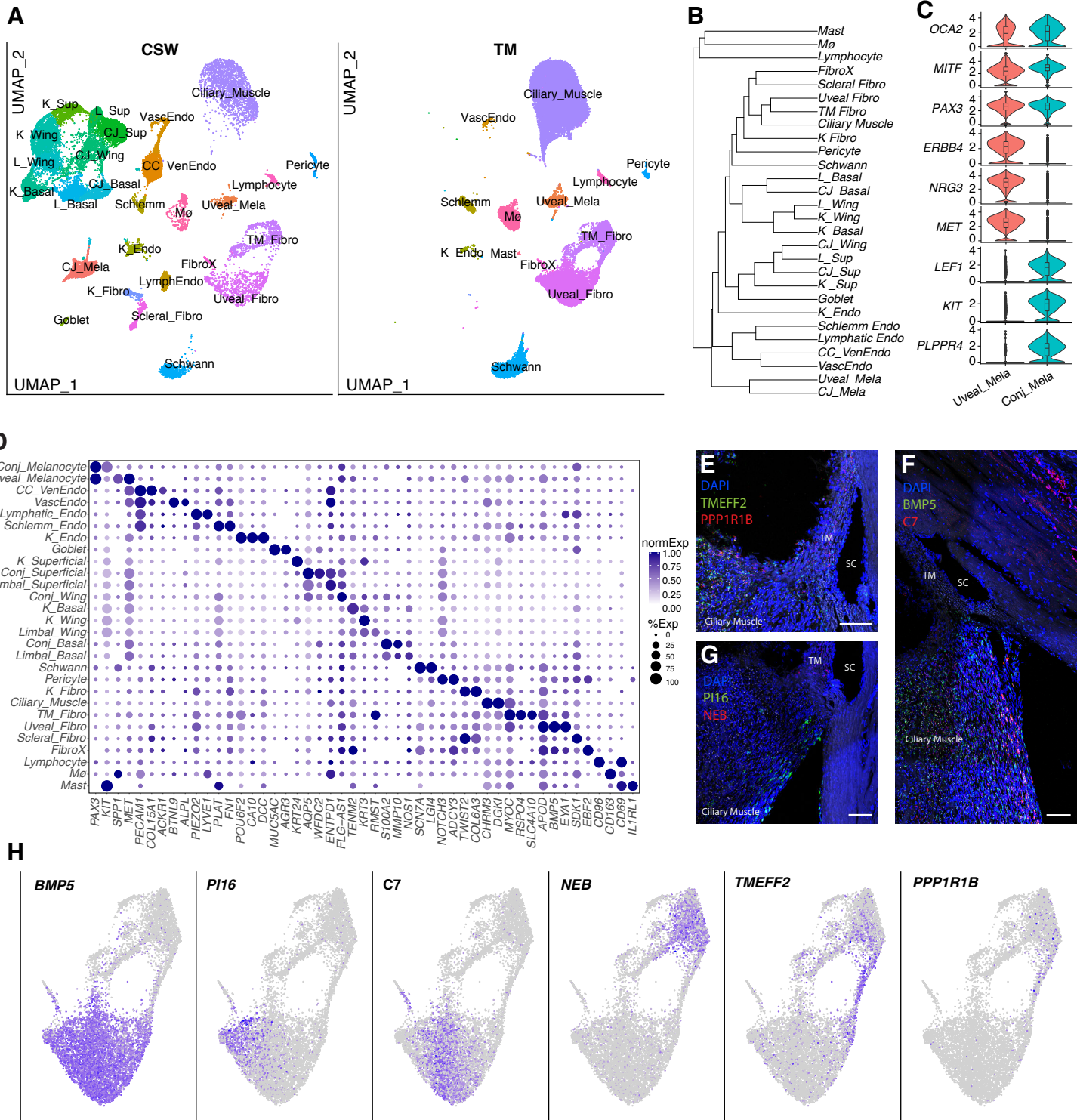


Fig. S4. Cell types of the Internal and External Limbus. (A) Clustering of 52,309 single-nucleus expression profiles derived from corneoscleral wedge (CSW) tissue visualized by UMAP. This panel shows contributions of cell types from the TM and CSW, which were processed separately and pooled for subsequent analysis. (B) Dendrogram demonstrates transcriptional relatedness among types. (C) Violin plots showing common and differentially expressed genes in conjunctival and uveal melanocytes. (D) Dot plot showing genes selectively expressed in cells of the internal and external limbus. (E) Fluorescent RNA in situ hybridization (ISH) for PPP1R1B (red) and TMEFF2 (green) highlights expression within cells of the TM as well as the ciliary muscle. (F) Fluorescent RNA ISH for C7 (red) and BMP5 (green) highlights expression within cells at the base of the TM and most prominently within the ciliary muscle. (G) Fluorescent RNA in situ hybridization for NEB (red) highlights cells confined to the TM and PI16 (green) highlights those within the ciliary body near the scleral interface. (H) Feature plots showing expression of a selection of genes discussed in a previous analysis of TM (van Zyl et al., 2020). Mo, macrophage; CJ, conjunctival; Vasc, vascular; Endo, endothelium; Fibro, fibroblast; K_Endo, corneal endothelium; TM, Trabecular Meshwork; K, corneal; L, Limbal; Mela, melanocyte; Sup, superficial. DAPI, 4',6-diamidino-2-phenylindole. Scale bars show 100 μ m.

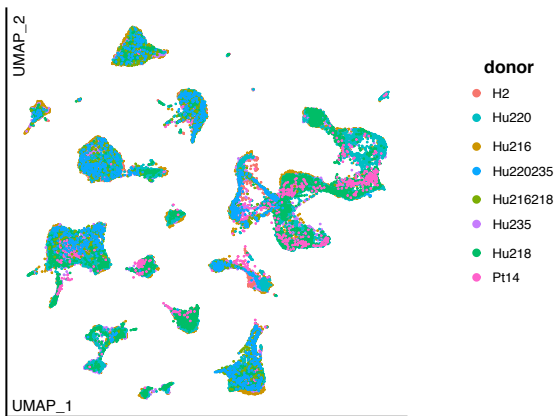
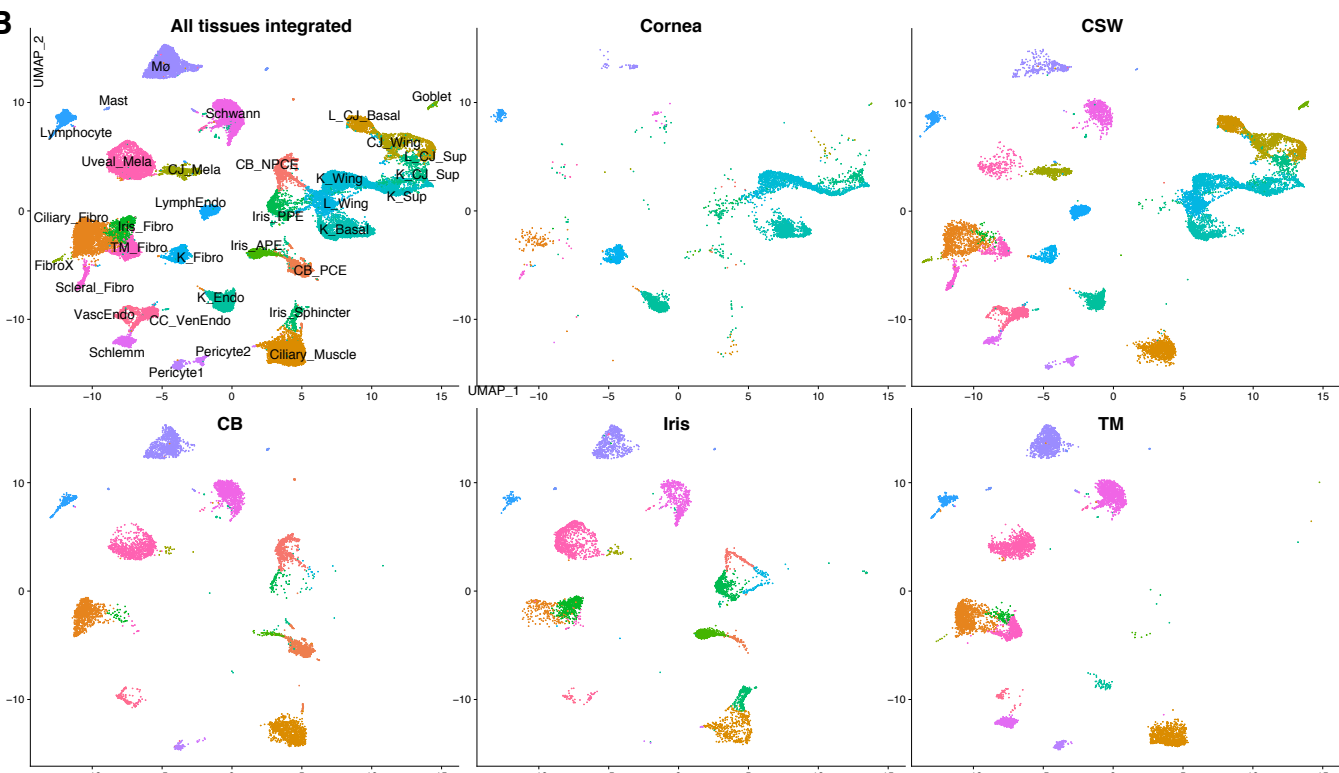
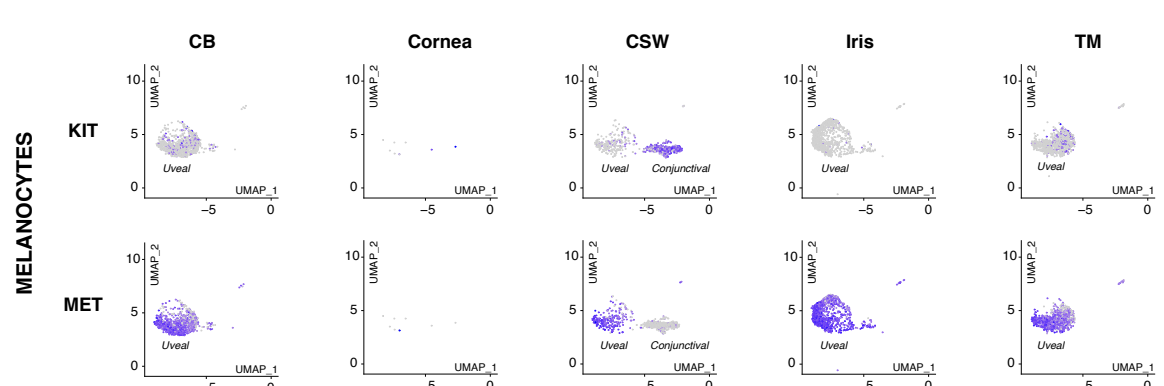
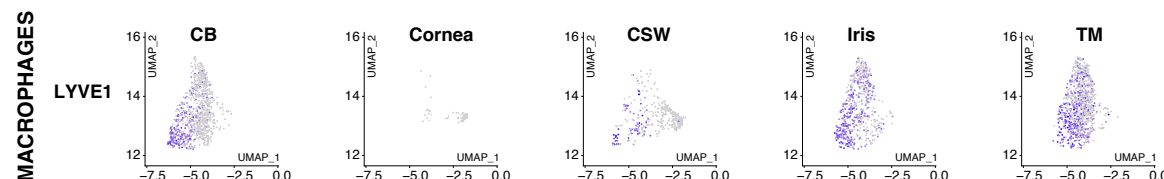
A**B****C****D**

Fig. S5. Integrated Analysis – Tissue and Donor Contributions. (A) Contributions of donor cells to each cluster as visualized by Uniform Manifold Approximation and Projection (UMAP) with individual colors representing unique donor source. Due to superposition effects, not all dots are visible. (B) Contributions of cells to integrated analysis by tissue source as visualized by UMAP. (C) Tissue sources of melanocyte cell types. All tissues except cornea contribute MET+ uveal melanocytes whereas KIT+ conjunctival melanocytes are exclusively derived from the CSW tissue. (D) Tissue sources of macrophages. Macrophage-type cells in the cornea and corneal portion of CWS are LYVE-negative, a pattern consistent across all donors.

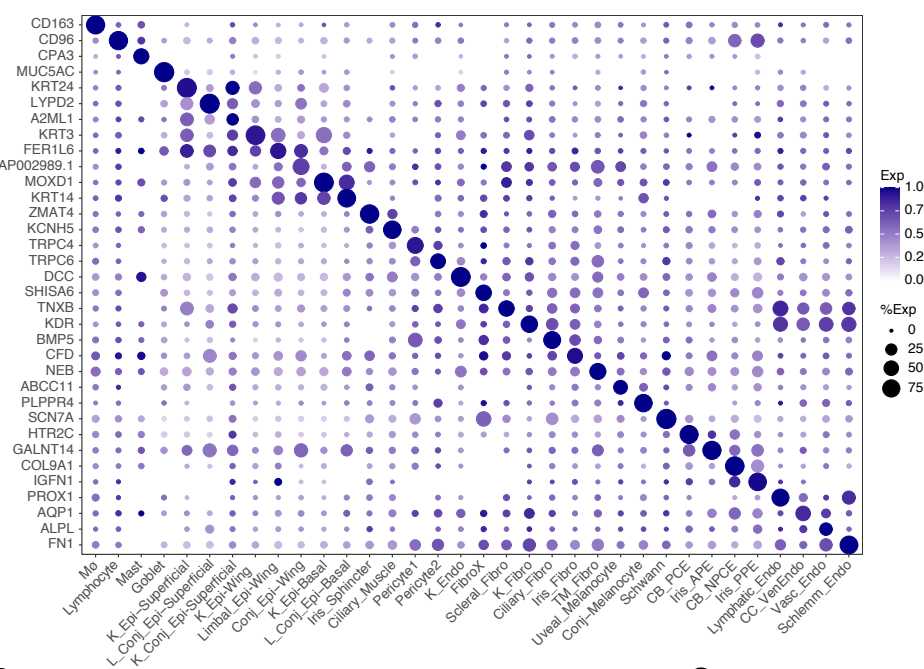
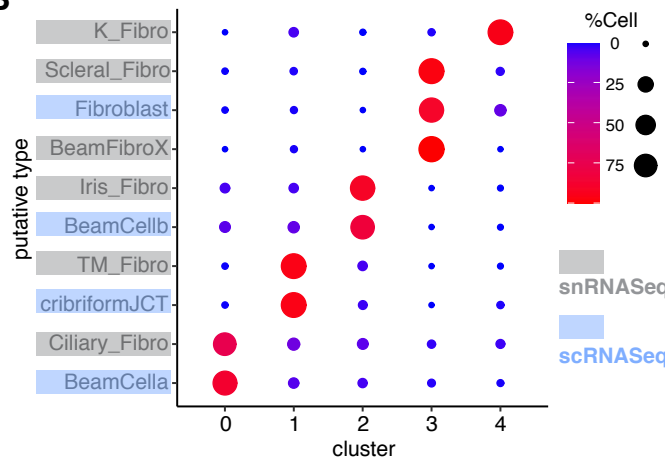
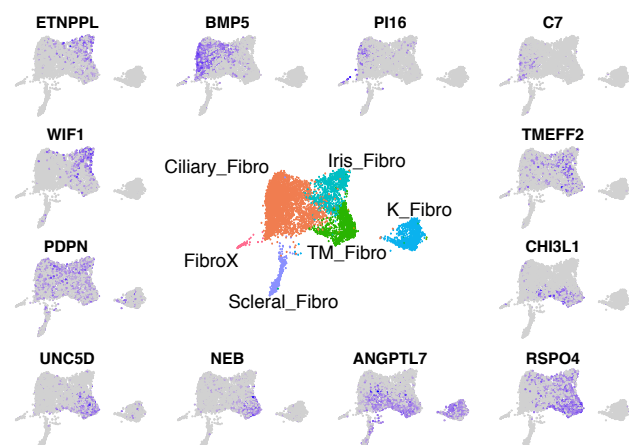
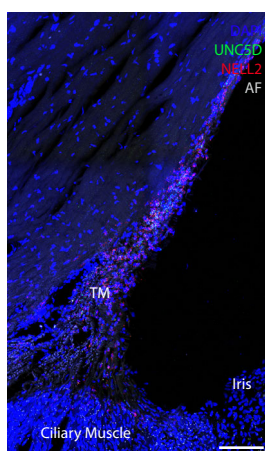
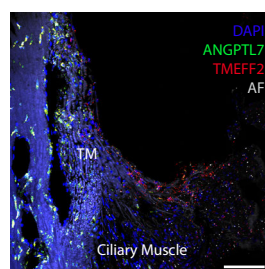
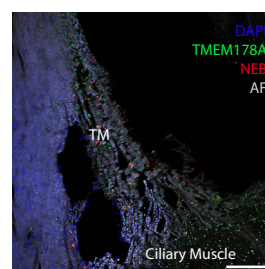
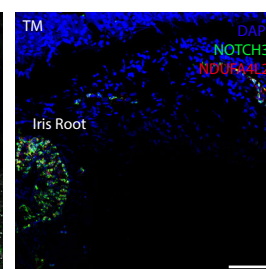
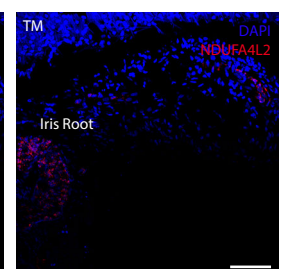
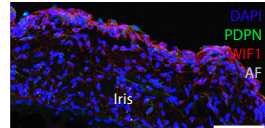
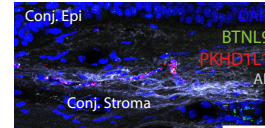
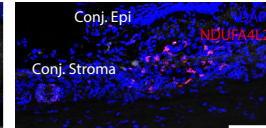
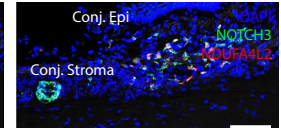
A**B****C****D****E****F****I****J****G****H****K****L**

FIG.S6. Integrated Analysis – Gene Expression and Histology. (A) Dot plot showing differentially expressed marker genes for each cell type in the integrated analysis. (B) Confusion plot demonstrating correspondence of fibroblast types in the current dataset with TM and fibroblast types in a previous scRNASeq report (23). scRNASeq and snRNASeq data were pooled and clustering was performed using methods as described for the main dataset. X-axis labels represent new clusters (putative types); y-axis labels represent the individual types included from each dataset. The size and color of the dots represent the proportion of cells/nuclei from each original cluster that were designated to one of the new five clusters. (C) Feature plots showing expression patterns of unique and shared genes within the fibroblast clusters. See Figure 5A for names of fibroblast types. (D) Fluorescent RNA in situ hybridization for *NELL2* (red) and *UNC5D* (green) highlights expression within TM fibroblasts confined to the trabecular meshwork. (E) Fluorescent RNA in situ hybridization for *TMEFF2* (red) highlights cells along the uveal border of the TM extending into the ciliary muscle and *ANGPTL7* (green) highlights those within the corneoscleral stroma and TM enriched in the juxtapacanicular region.

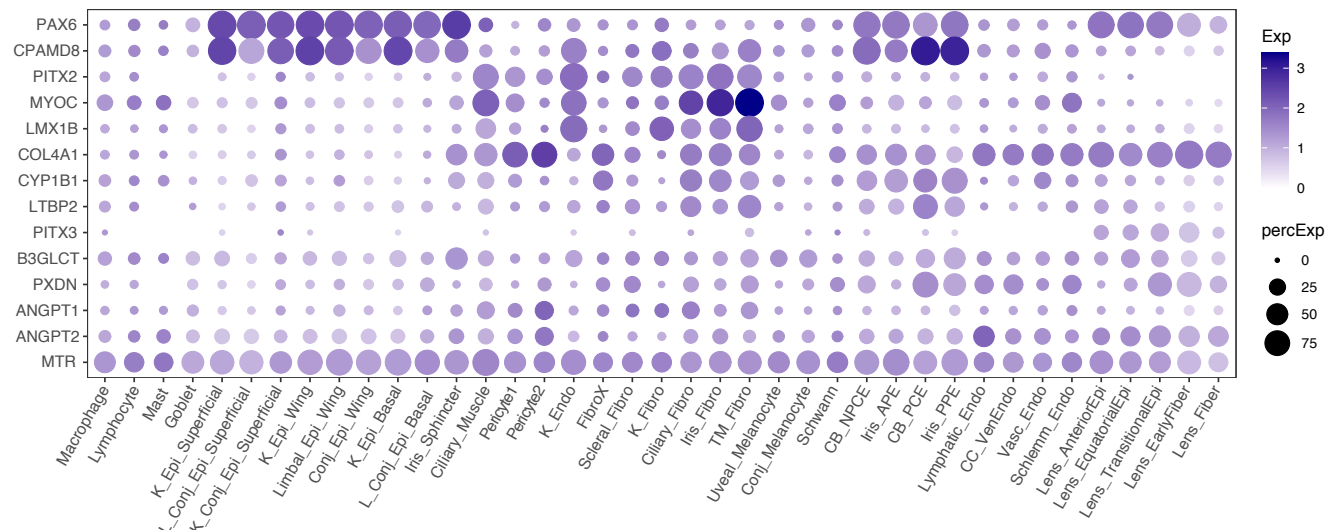
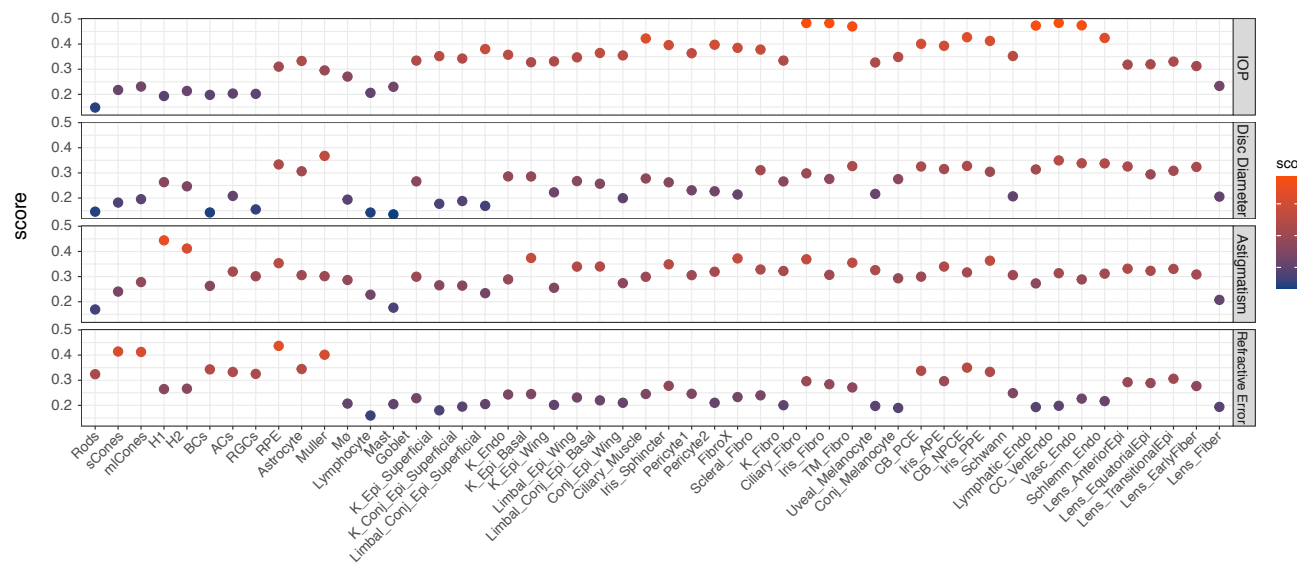
A**B**

FIG. S7. Human Disease Genes. (A) Dot plot showing expression patterns of select genes implicated in anterior segment dysgenesis, cataract, glaucoma and ectopia lentis within the anterior segment and lens. (B) Dot plot showing cell-type specific enrichment scores of genes identified through GWAS for common ocular conditions or traits. Major retinal cell types from non-diseased human macular samples are also included. Similar plots for other disease states are shown in Figure 6D. CB, Ciliary Body; NPCE, non-pigmented ciliary epithelium; pigmented ciliary epithelium; RPE, Retinal Pigment Epithelium; H1/H2, Horizontal Cells; BC, Bipolar Cells; AC, Amacrine Cells; RGC, Retinal Ganglion Cells; K, cornea; CC, collector channel; Epi, Epithelium, Endo, Endothelium, Conj, Conjunctiva, Fibro, fibroblast, PPE, posterior pigmented epithelium, Mø, macrophage.

Fig. S8A Astigmatism

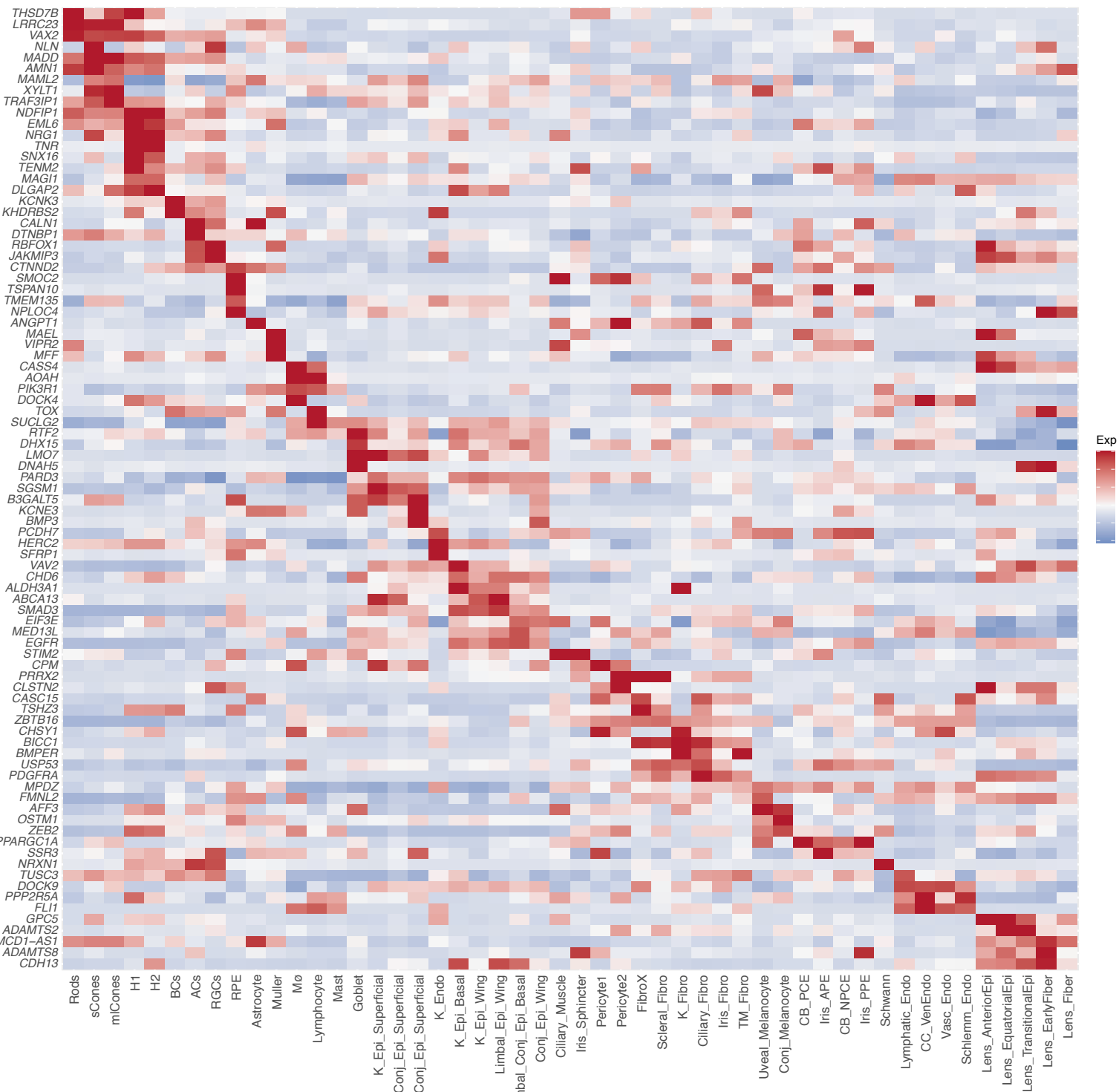


Fig. S8B Disc Diameter

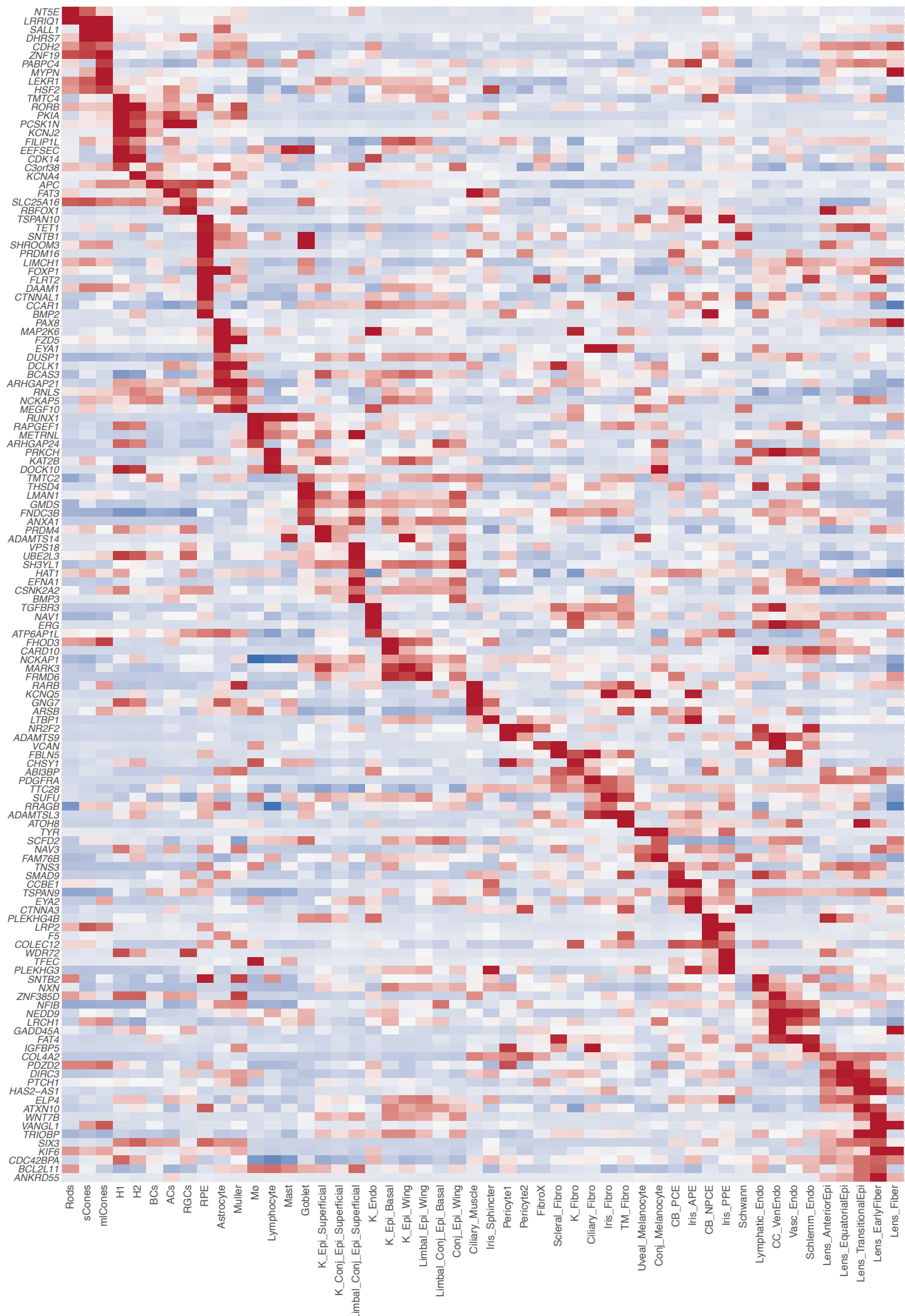


Fig. S8C Intraocular Pressure (IOP)

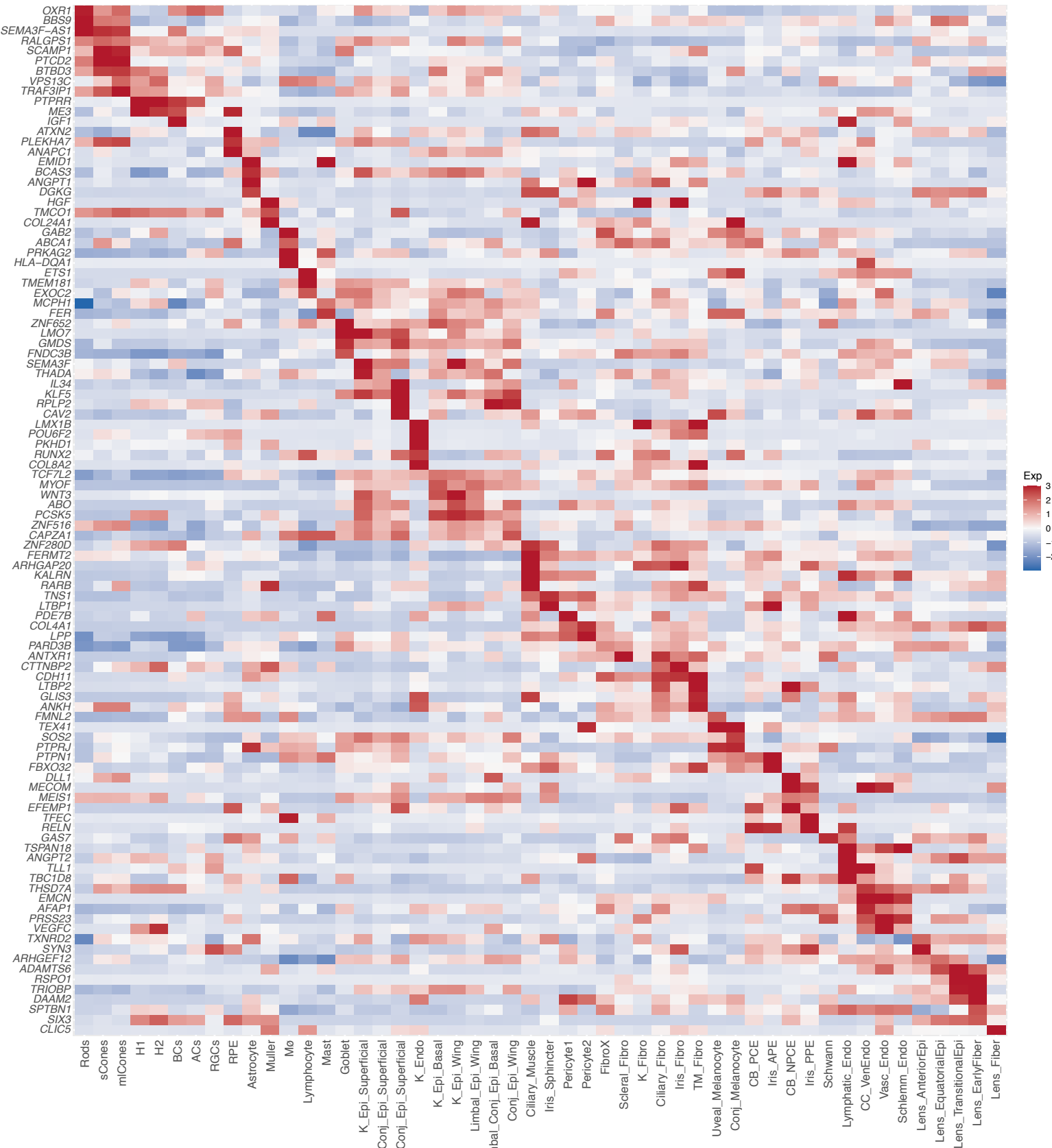


Fig. S8D Myopia

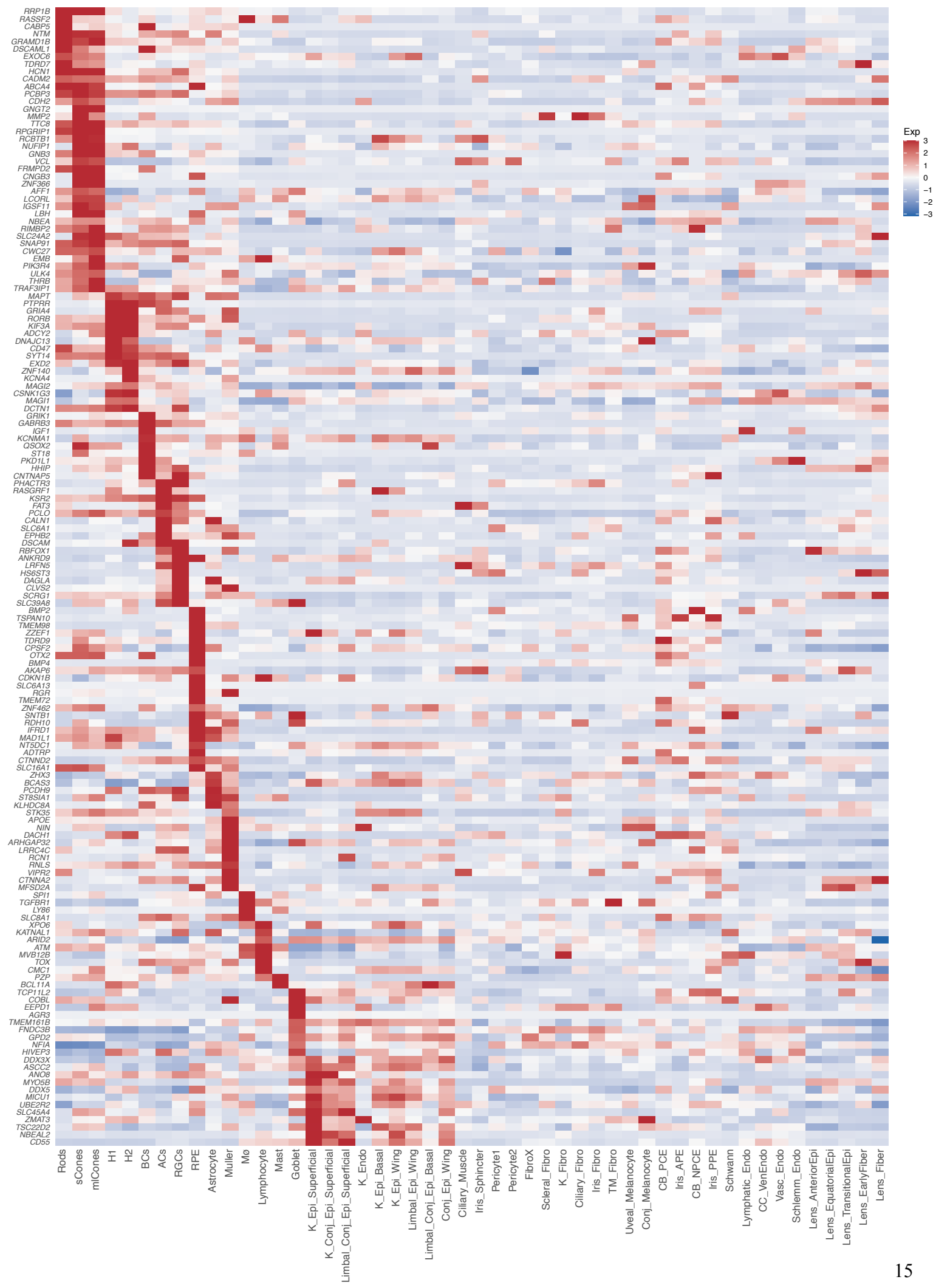


Fig. S8D Myopia (Continued)

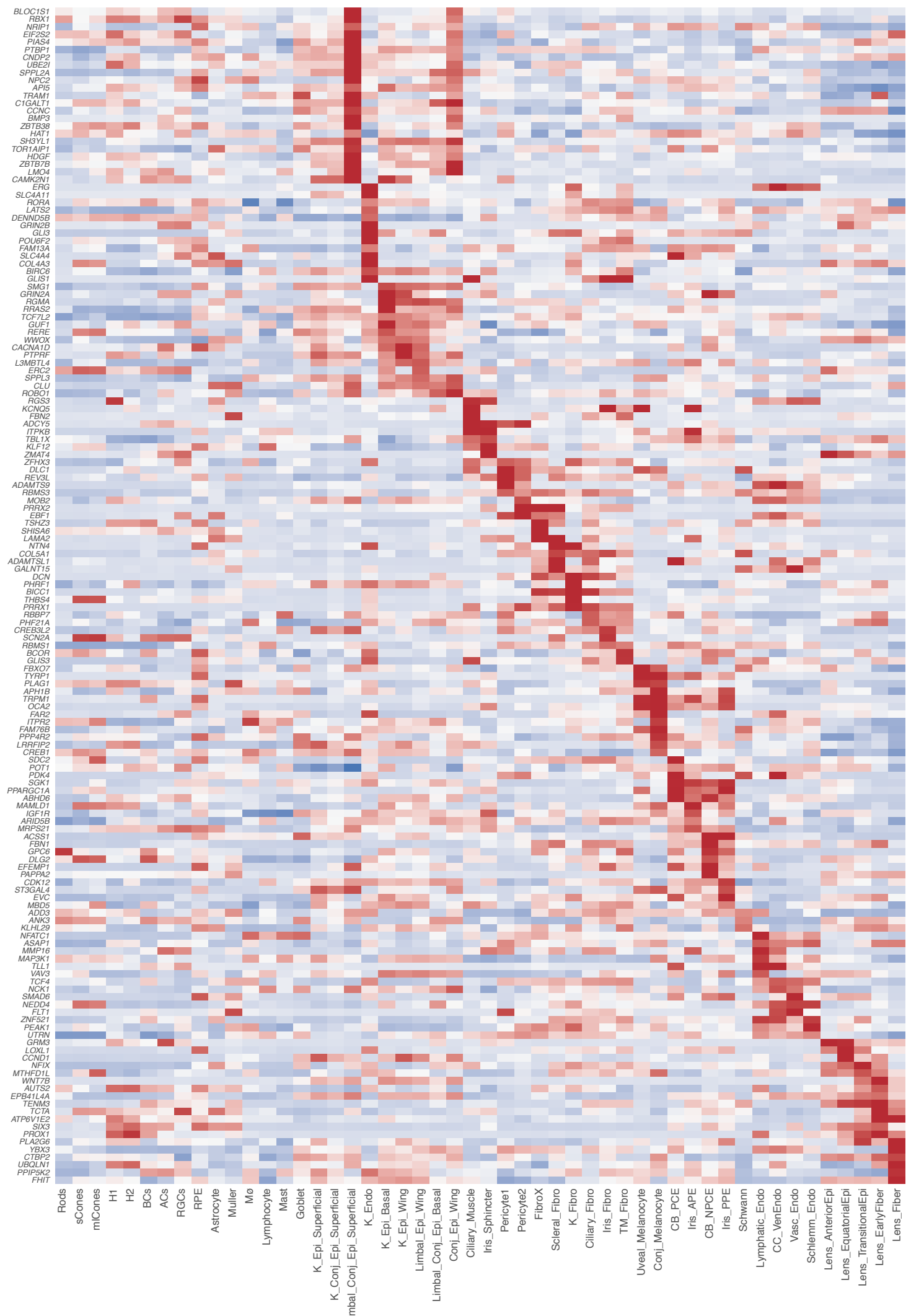


Fig. S8E Primary Open Angle Glaucoma (POAG)

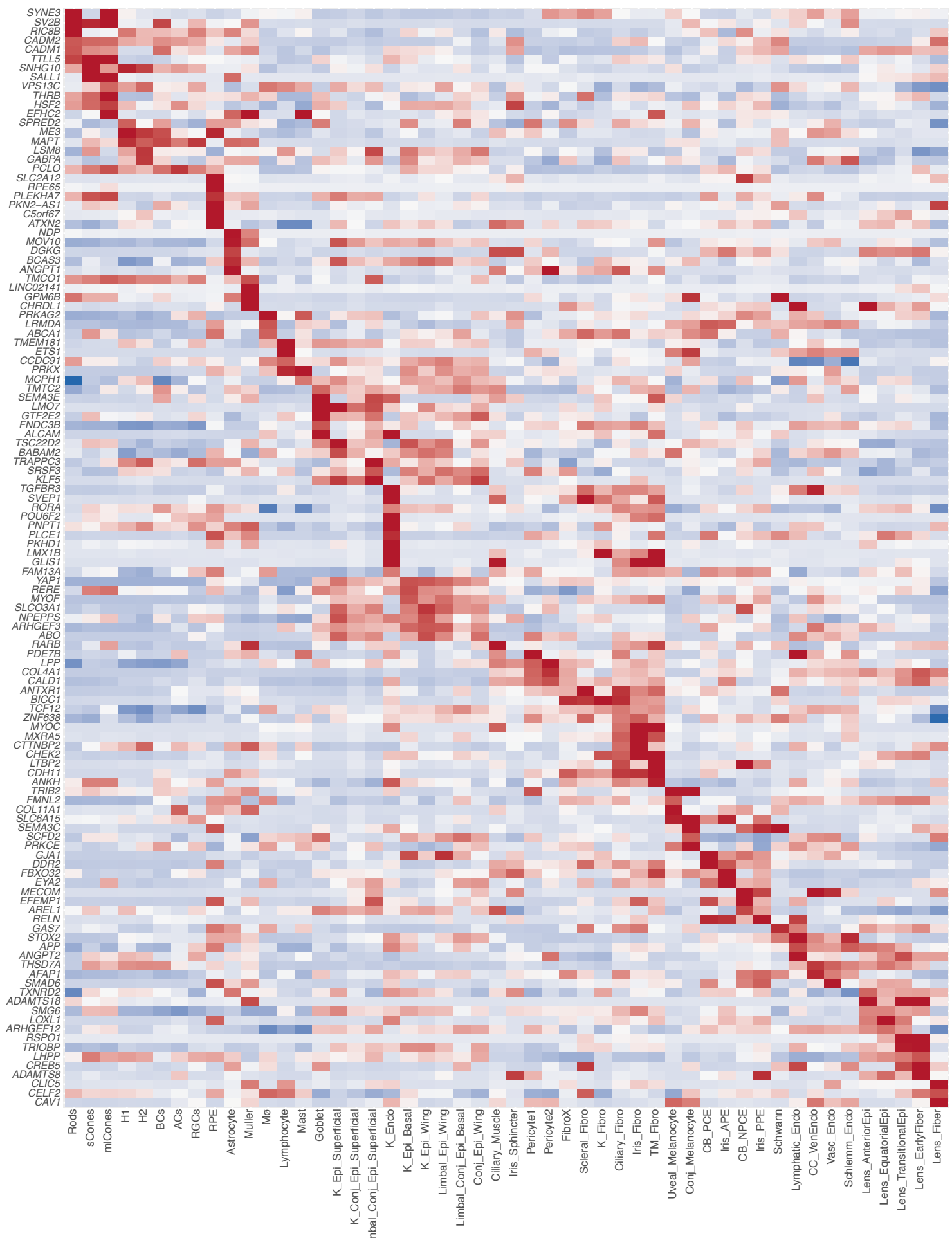


Fig. S8F Refractive Error

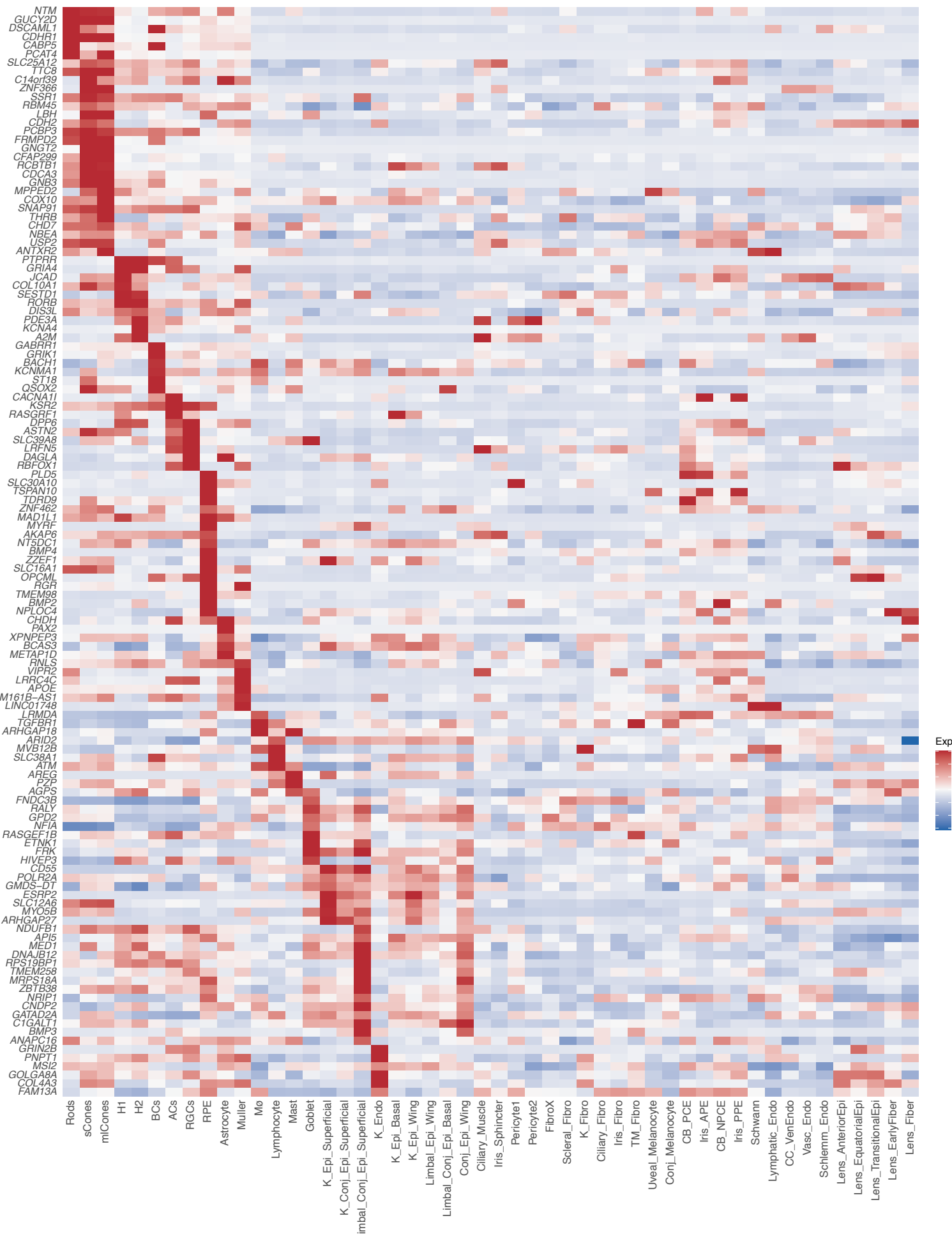


Fig. S8F Refractive Error (Continued)

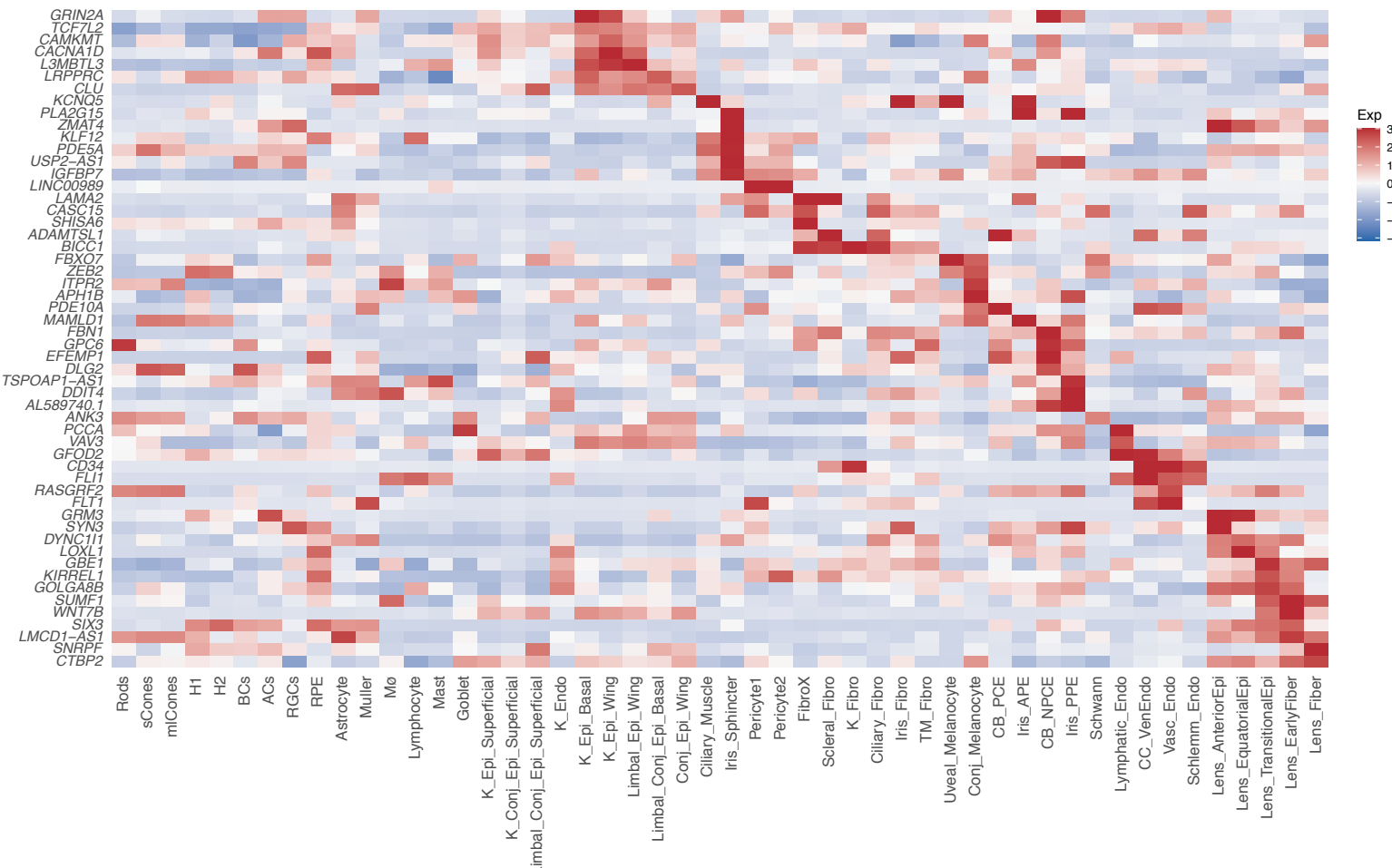
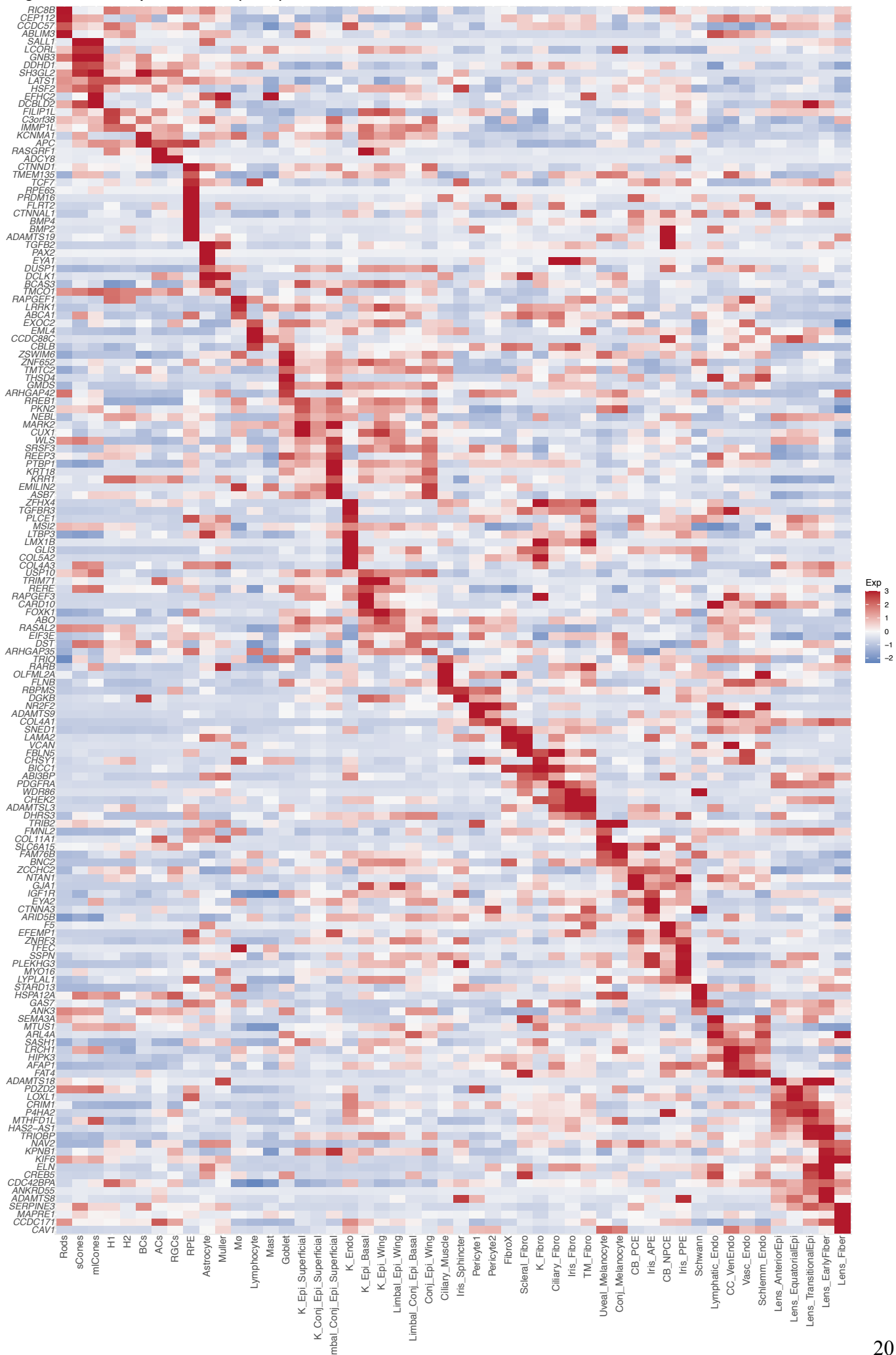


Fig. S8G Vertical Cup to Disc Ratio (VCDR)



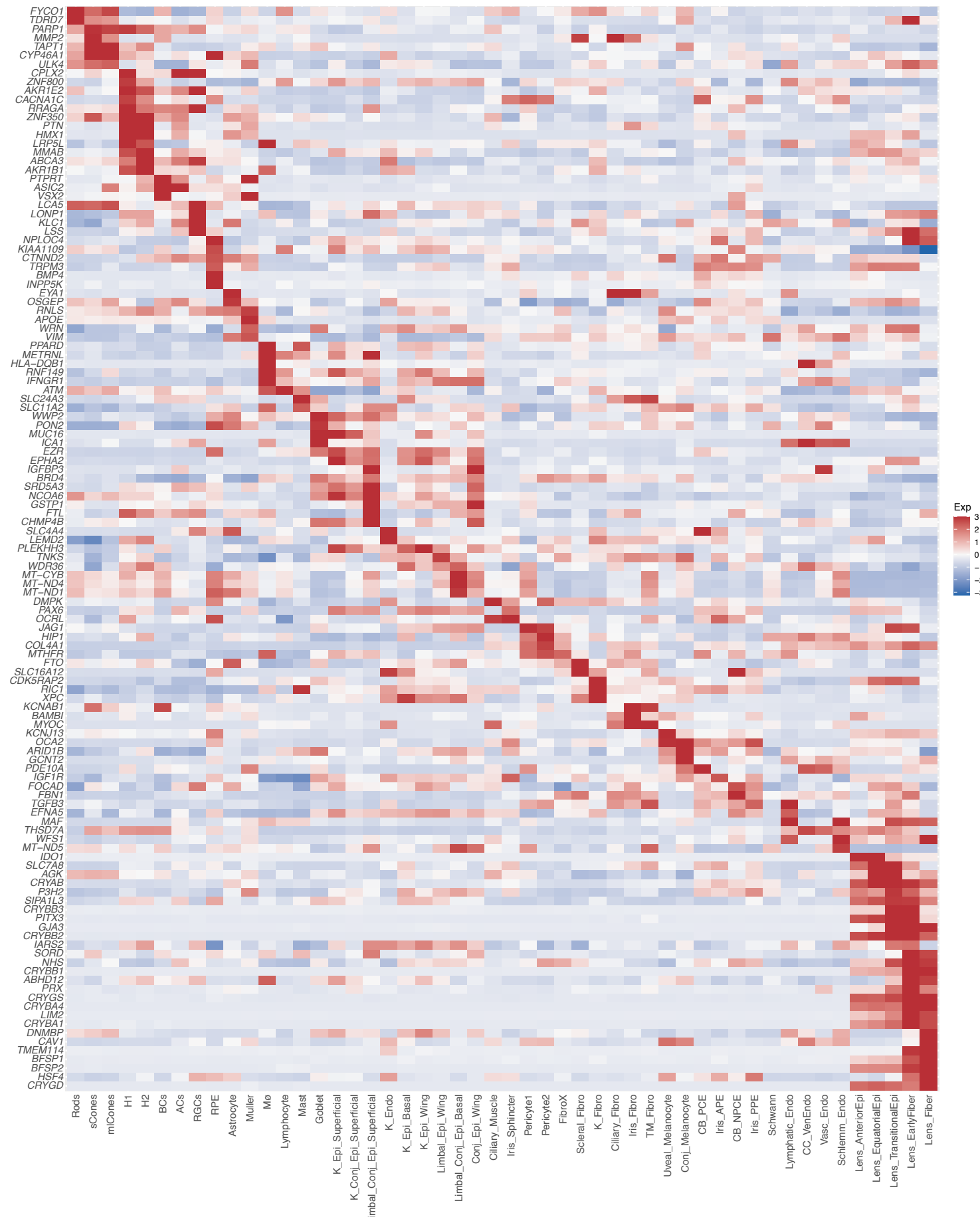


Fig. S8. Human Disease Genes. Heatmap showing row-normalized expression of genes implicated in susceptibility to ocular disease or in phenotypes related to disease. For improved visualization of expression level differences among types across a large group of genes, normalized values above 3 were set to 3. In most cases, genes were identified through GWAS, but some Mendelian genes are also included. The genes in the heatmap were used the expression scores for corresponding conditions or traits shown in Fig. 6D and S7B. (A) Astigmatism; (B) Variations in optic disc diameter; (C) Elevated intraocular pressure; (D) Myopia; (E) Primary open angle glaucoma; (F) Refractive error; (G) Vertical cup to disc ratio; (H) Cataract.

Supplementary Table 1. Donor Information (RNAseq)

Label	Source	Age	Sex	Cause of Death	DTP (hours)	Tissues processed for RNAseq (10X version chemistry)
Pt2 Rt	MGH	78	M	Metastatic melanoma to brain	14	CB(V3)
Pt14-Rt	MGH	33	M	Colorectal cancer	4	Lens(V3.1)
0216-20 OD	UT	66	F	Sepsis, end stage liver disease	4.5	CB(V3) Iris(V3.1)
0216-20 OS	UT	66	F	Sepsis, end stage liver disease	4.5	Cornea(V3), Iris(V3.1), CSW(V3.1), TM(V3.1) Lens (V3.1)
0218-20 OS	UT	65	M	Cardiogenic shock	5.5	TM(V3.1), Lens(V3.1), Cornea(V3), Iris(V3.1) CSW(V3.1), Macula (V3.1)
0220-20 OS	UT	47	F	Metastatic brain cancer	3.5	TM(V3.1), Lens(V3.1), Cornea(V3), Iris(V3.1) CSW(V3.1), CB(V3)
0235-20 OS	UT	30	M	Respiratory failure	5	TM(V3.1), Lens(V3.1), Cornea(V3), Iris(V3.1) CSW(V3.1), CB(V3)
0822-19	UT	41	M	Acute Cardiac Event	5.3	Macula (V3.1)
0326-16	UT	67	M	Sepsis	5	Macula (V3.1)
0563-16	UT	72	M	Anoxic Brain Injury	5.25	Macula (V3.1)
0887-16	UT	77	M	Sepsis	5.75	Macula (V3.1)

DTP = Death to Processing Time

Supplementary Table 2. Donor Information (Histology)

Label	Source	Age	Sex	COD	DTP (hr)	RNA <i>in situ</i>	IHC
1041-16	Utah	43	F	Sepsis	5.5	N/A	PDPN, PECAM1, DES, AQP1
1094-20	Utah	58	M	Pancreatic cancer	3.5	ANGPTL7, BCAS1, LGR6, MECOM, PDGFC, NTRK2	AQP1, RELN, LRP2
Pt9-IrcB	MGH	53	F	Interstitial Lung Disease	5	N/A	CRB1, PDPN, PECAM1
1093-20	Utah	66	F	Cardiac arrest	4.5	MECOM, LGR6, KRT12, RARRES1, CACNA1A, ATP8B4, BCAS1, NECTIN4, TOP2A, LAMA3, UCHL1, SLC1A2, GRIA4, ETNPPL, GPR160, CAV1	MLANA, MUC5AC
Pt7-K	MGH	52	F	Brain hemorrhage; metastatic brain cancer	4	N/A	KRT78
HCS13	Lions	22	F	Cystic Fibrosis	10	N/A	MLANA
0414-21	Utah	30	M	Cardiac Arrest	4.5	BMP5, C7, PI16, NEB, PPP1R1B, TMEFF2, UNC5D, NELL2, PKHD1L1, FN1	N/A
0245-21	Utah	60	F	Respiratory Arrest	4.5	NOTCH3, ID4, NDUFA4L2, ADCY3, WFDC2, ENTPD1, BMP5, ETNPPL, PAX3, MET, KIT, LEF1, FN1, GRIA4, ANGPTL7, PPP1R1B	N/A

DTP = Death to Processing Time

Supplementary Table 3. Antibody & RNA *in situ* Probe Information

Antibody/Probe	Supplier	Catalog #
Sheep Polyclonal anti-Podoplanin	R&D Systems	AF3670
Rabbit Polyclonal anti-CD31/PECAM-1	Novus Biologicals	NB100-2284
Goat Polyclonal anti-Desmin	R&D Systems	AF3844
Rabbit Polyclonal anti-Aquaporin-1	Proteintech	20333-1-AP
Rabbit Polyclonal anti-LRP2	Lifespan Biosciences	LS-B15008
Mouse Monoclonal anti-Reelin	Developmental Studies Hybridoma Bank	TB5
Rabbit Polyclonal anti-CRB1	Bioss Antibodies	BS-14045R
Mouse Monoclonal anti-Melan-A	Proteintech	60348-1-Ig
Mouse Monoclonal anti-Mucin 5AC	Abcam	ab3649
Rabbit Polyclonal anti-Keratin 78	Novus Biologicals	NBP1-93671
Rabbit Polyclonal anti-CA3	Lifespan Biosciences	LS-B9781
RNAscope® Probe-Hs-ANGPTL7	Advanced Cell Diagnostics	552811
RNAscope® Probe-Hs-BCAS1	Advanced Cell Diagnostics	525781-C3
RNAscope® Probe-Hs-LGR6	Advanced Cell Diagnostics	410461-C2
RNAscope® Probe-Hs-MECOM	Advanced Cell Diagnostics	518021
RNAscope® Probe-Hs-PDGFC	Advanced Cell Diagnostics	404281
RNAscope® Probe-Hs-NTRK2	Advanced Cell Diagnostics	402621-C2
RNAscope® Probe-Hs-KRT12	Advanced Cell Diagnostics	506311-C2
RNAscope® Probe-Hs-RARRES1	Advanced Cell Diagnostics	494851
RNAscope® Probe-Hs-CACNA1A	Advanced Cell Diagnostics	558581
RNAscope® Probe-Hs-ATP8B4	Advanced Cell Diagnostics	Custom ¹
RNAscope® Probe-Hs-NECTIN4	Advanced Cell Diagnostics	562061
RNAscope® Probe-Hs-TOP2A	Advanced Cell Diagnostics	470321
RNAscope® Probe-Hs-LAMA3	Advanced Cell Diagnostics	530681
RNAscope® Probe-Hs-UCHL1	Advanced Cell Diagnostics	594281
RNAscope® Probe-Hs-SLC1A2	Advanced Cell Diagnostics	444721-C3

RNAscope® Probe-Hs-GRIA4	Advanced Cell Diagnostics	464671
RNAscope® Probe-Hs-ETNPLL	Advanced Cell Diagnostics	492121-C3
RNAscope® Probe-Hs-GPR160	Advanced Cell Diagnostics	482681
RNAscope® Probe-Hs-CAV1	Advanced Cell Diagnostics	452071-C2
RNAscope® Probe-Hs-BMP5	Advanced Cell Diagnostics	472461
RNAscope® Probe-Hs-C7	Advanced Cell Diagnostics	534791-C3
RNAscope® Probe-Hs-PI16	Advanced Cell Diagnostics	569181
RNAscope® Probe-Hs-NEB	Advanced Cell Diagnostics	554391-C3
RNAscope® Probe-Hs-PPP1R1B	Advanced Cell Diagnostics	477021-C2
RNAscope® Probe-Hs-TMEFF2	Advanced Cell Diagnostics	519741
RNAscope® Probe-Hs-UNC5D	Advanced Cell Diagnostics	459991
RNAscope® Probe-Hs-NELL2	Advanced Cell Diagnostics	Custom ²
RNAscope® Probe-Hs-PKHD1L1	Advanced Cell Diagnostics	Custom ³
RNAscope® Probe-Hs-BTNL9	Advanced Cell Diagnostics	430351
RNAscope® Probe-Hs-FN1	Advanced Cell Diagnostics	310311-C2
RNAscope® Probe-Hs-NOTCH3	Advanced Cell Diagnostics	558991-C2
RNAscope® Probe-Hs-ID4	Advanced Cell Diagnostics	466371-C3
RNAscope® Probe-Hs-NDUFA4L2	Advanced Cell Diagnostics	567011-C3
RNAscope® Probe-Hs-ADCY3	Advanced Cell Diagnostics	441671
RNAscope® Probe-Hs-WFDC2	Advanced Cell Diagnostics	524781
RNAscope® Probe-Hs-ENTPD1	Advanced Cell Diagnostics	474181-C2
RNAscope® Probe-Hs-PAX3	Advanced Cell Diagnostics	562711-C2
RNAscope® Probe-Hs-MET	Advanced Cell Diagnostics	431021-C3
RNAscope® Probe-Hs-KIT	Advanced Cell Diagnostics	606401-C3
RNAscope® Probe-Hs-LEF1	Advanced Cell Diagnostics	412991

¹ 20 ZZ probe targeting 1119-2158 of NM_024837.4

² 20 ZZ probe targeting 668-1660 bp of NM_001145108.2

³ 20 ZZ probe targeting 4456-5459 bp of NM_177531.6

Dataset S1 (separate file). Differentially expressed (DE) genes for cell types in the anterior segment. File contains separate tabs for each of the tissues profiled, including Central cornea, TM/CSW, Iris, Ciliary Body, and Lens, as well as a tab with the DE genes identified during the integrated analysis.

SI References

1. T. van Zyl *et al.*, Cell atlas of aqueous humor outflow pathways in eyes of humans and four model species provides insight into glaucoma pathogenesis. *Proc Natl Acad Sci U.S.A.* **117**, 10339-10349 (2020).
2. X. Han *et al.*, Automated AI labeling of optic nerve head enables insights into cross-ancestry glaucoma risk and genetic discovery in > 280,000 images from UKB and CLSA. *Am. J. Hum. Genet.* **108**, 1204-1216 (2021).
3. P. Gharahkhani *et al.*, Genome-wide meta-analysis identifies 127 open-angle glaucoma loci with consistent effect across ancestries. *Nat. Commun.* **12**, 1-6, (2021).
4. A.P. Khawaja *et al.*, Genome-wide analyses identify 68 new loci associated with intraocular pressure and improve risk prediction for primary open-angle glaucoma. *Nat. Genet.* **50**, 1–11 (2018).
5. P.G. Hysi *et al.*, Meta-analysis of 542,934 subjects of European ancestry identifies new genes and mechanisms predisposing to refractive error and myopia. *Nat. Genet.* **52**, 401–407 (2020).
6. A. Buniello *et al.*, The NHGRI-EBI GWAS Catalog of published genome-wide association studies, targeted arrays and summary statistics 2019. *Nucleic Acids Res.* **47**, D1005-D1012 (2019).
7. A. Shiels, T.M Bennett, J.F. Heitmancik, Cat-Map: putting cataract on the map. *Mol. Vis.* **16**, 2007–2015 (2010).